Metals

Hot workability and microstructure evolution of Al–0.2Sc–0.04Zr alloy

Yong Xue[1,*] ⓘ, Shuaishuai Chen[1], Zhimin Zhang[1], Qiang Wang[1], and Jiangpeng Yan[1]

[1] School of Material Science and Engineering, North University of China, No. 3 Xueyuan Rd., Taiyuan 030051, China

ABSTRACT

Hot deformation behavior of Al–0.2Sc–0.04Zr (wt.%) aluminum alloy was investigated via conducting hot compression tests at temperatures of 440–600 °C and at strain rates, ranging from 0.001 to 5 s^{-1}, at an interval of an order of magnitude. The characteristics of the true stress–strains acquired in the hot compression tests were investigated, and the influence of processing parameters on the microstructure of the deformed samples was observed by using optical microscope and electron back-scattered diffraction (EBSD). Two types of processing maps for Al–0.2Sc–0.04Zr alloy were developed using the Kumar–Prasad (K–P) and Murty–Rao (M–R) instability/stability criteria, respectively. The prediction results of two types of processing maps were examined. Based on the analysis of the M–R processing map and EBSD, a deformation mechanism map covering a wide range of temperature and strain rate was developed. The result shows that the flow stress had a rapid increase to the maximum stress, and subsequently, the flow stress decreases continually to be of steady-state type when the deformation continues on. The M–R criterion can more accurately predict the unstable region than the K–P criterion. The optimum temperature T and strain rate $\dot{\varepsilon}$ combination conditions for Al–0.2Sc–0.04Zr alloy are $T = 520$–560 °C, $\dot{\varepsilon} = 10^{-3}$ s^{-1} or $\dot{\varepsilon} = 0.1$–5 s^{-1}. The microstructure evolution dominated by the predominant or complete dynamic recrystallization can be acquired by deformation at the combination conditions. However, it is dominated mainly by dynamic recovery at lower temperatures ($T < 520$ °C) and by dynamic recrystallization at higher temperatures ($T > 520$ °C). In addition, the microstructure of specimen deformed at 600 °C shows a growing and coarse trend. Moreover, the nano-dimension precipitate particles of $Al_3(Sc,Zr)$ are uniformly distributed throughout Al matrix. The efficiency parameter η value of Al–0.2Sc–0.04Zr alloy in processing maps is smaller in comparison with that in pure aluminum, and it could be attributed to these nano-dimension particles.

Address correspondence to E-mail: yongxue395@163.com

Introduction

Due to its superior mechanical properties, thermal stability, high-temperature conductivity, corrosion resistance and creep resistance, the Al–0.2Sc–0.04Zr alloy has become a popular candidate material for the development of new super-heat-resistant wires [1, 2]. Researches show that, after cold working deformation and aging treatment, the strength of the Al–0.2Sc–0.04Zr alloy improves significantly to more than 200 MPa [3, 4]. Its conductivity exceeds 35.76 MS/m, and its maximal operation temperature exceeds 300 °C [5], which is significantly higher than the operation temperature of current heat-resistant aluminum wires 150 °C. And the $Al_3(Sc,Zr)$ is not easy to coarsening even at high temperature of 550 °C [7], which helps to maintain the beneficial property of $Al_3(Sc,Zr)$ at high temperature. The precipitate particles of $Al_3(Sc,Zr)$ are usually dispersed throughout the Al matrix at a high density, increasing the recrystallization temperature and the strength of the alloy [6, 7, 8], which also enhance corrosion resistance and creep resistance properties [8].

Controlling the microstructures of wires is the key to controlling their properties, including their mechanical properties, creep resistance, corrosion resistance and so on. A processing map is an important tool for optimizing the thermal processing parameters of metallic materials. For different processing conditions, the processing map is usually used to evaluate the particular microstructure deformation mechanisms [9], which include dynamic recovery (DRV), dynamic recrystallization (DRX), the presence of adiabatic shear bands (ASBs), flow localization, the formation of wedge cracks. Processing maps help researchers master useful material processing information, predict unstable regions that should be avoided during thermal deformation, optimize processing parameters, precisely control structures, and avoid defects [10]. Currently, the majority of the research studies on the Al–0.2c–0.04Zr alloy focus on the following two areas: (1) the effect of Sc and Zr on the aluminum alloy properties [1, 4, 7] and (2) the effect of heat treatment processes [11, 12] (homogeneous annealing and aging treatment, among others) or thermal mechanical treatment processes [2, 3] (hot extrusion + aging treatment and cold rolling + aging treatment, among others) on the chemical and mechanical properties and conductivity of the Al–Sc–Zr alloy. However, there are few reports on high-temperature flow behavior, processing map and microstructure evolution. Since Al–0.2Sc–0.04Zr has tremendous commercial potential for high-strength, super-heat-resistant wire for aerial materials, its high-temperature flow behavior under various processing conditions should be investigated thoroughly to achieve optimal performance control.

In the present work, we developed two types of processing maps for Al–0.2Sc–0.04Zr from the flow curves measured during hot compression over wide ranges of forming temperature and strain rate using two common instability/stability criteria, the Kumar–Prasad (K–P) and Murty–Rao (M–R) criteria. The Kumar–Prasad (K–P) instability criterion is defined as follows:

$$\xi(\dot{\varepsilon})_{K-P} = \frac{\partial \ln(m/(m+1))}{\partial \ln \dot{\varepsilon}} + m < 0 \tag{1}$$

Strictly speaking, the K–P instability criterion is correct only when the flow stress versus strain rate $(\sigma - \dot{\varepsilon})$ obeys the constitutive relation $\sigma = K\dot{\varepsilon}^m$ in which m is independent of $\dot{\varepsilon}$. However, Murty and Rao [13, 14] assumed that m should not be a constant and thus developed another instability criterion applicable for any relation of the $(\sigma - \dot{\varepsilon})$ curve. The Murty–Rao (M–R) instability criterion is,

$$\xi(\dot{\varepsilon})_{M-R} = 2m - \eta < 0 \tag{2}$$

The efficiency parameter, η, can be defined as:

$$\eta = \frac{J}{J_{max}} = \frac{\frac{m}{m+1}\sigma\dot{\varepsilon}}{\frac{\sigma\dot{\varepsilon}}{2}} = \frac{2m}{m+1} \tag{3}$$

In addition, through microstructure verification of the two processing maps, we wanted to confirm a more accurate processing map for the Al–0.2Sc–0.04Zr alloy. The detailed microstructure evolution and distribution of precipitated phases were examined by employing electron back-scattered diffraction (EBSD), scanning electron microscopy (SEM) and energy-dispersive spectroscopy (EDS). As a supplement, the deformation mechanism map and the superior heat resistance of this alloy were developed and discussed, respectively.

Experimental procedure

The Al–0.2Sc–0.04Zr alloy in this study were prepared by melting method, and its chemical composition is listed in Table 1. Prior to hot compressive

Table 1 Chemical composition of the Al–0.2Sc–0.04Zr alloy (wt.%)

Sc	Zr	Ar	Fe	Si	Al
0.190	0.038	0.120	0.002	0.001	Balance

test, the homogenized annealing treatment was carried out at 630 °C for 6 h to eliminate composition segregation. The cylindrical samples with circular cross section of Φ8 mm and 12 mm in height were machined from the annealed material. Isothermal compression tests with a true strain of 0.8 were carried out on a Gleeble-1500D thermomechanical simulator at five different temperatures (440 °C, 480 °C, 520 °C, 560 °C and 600 °C) and at five different strain rates (0.001 s^{-1}, 0.01 s^{-1}, 0.1 s^{-1}, 1 s^{-1} and 5 s^{-1}). During compression, graphite sheets were placed at both ends of the sample to reduce friction between the sample and the pressure head. Samples were in situ water quenched immediately after deformation. The compressed samples were cut down the middle along the compression axis (Fig. 1a) to produce longitudinal sections which were used for microstructure observation (Fig. 1b). The observation area was limited to a central region to ensure accurate microstructure analysis (Fig. 1b). After sand grinding and mechanical polishing, the observational surfaces were corroded by HF acid (5% v/v) for about 60 s. The optical microstructures were observed using a ZEISS PL-A662 digital optical microscope (OM). A VibroMet™2 vibration polisher was employed to polish the observational surfaces until stress-free glossy surfaces were produced. A Hitachi SU5000 SEM was employed for the observation of

precipitated phase, EDS analysis and EBSD data collection. The EBSD data (confidence index > 0.2) were analyzed using TSL-OIM analysis software and Origin software (Table 1).

Results and discussion

Hot deformation characteristics

True stress–strain curves

The flow stress–strain curves can be divided into two types: DRV and DRX [15] ,in accordance with the dynamic softening mechanisms that occur during hot deformation. Figure 2a shows the true stress–strain curves of the Al–0.2Sc–0.04Zr alloy deformed at various deformation temperatures at strain rate of 0.1 s^{-1}. Figure 2b shows the sketch of DRX-type curve, which usually consists of the following three different stages [16], including the work-hardening stage (stage I), dynamic flow softening stage (stage II) and steady stage (stage III). The typical DRX-type curve assumes that dynamic recrystallization is mainly its softening mechanism. From Fig. 2a, it can be seen that the true stress–strain curve of Al–0.2Sc–0.04Zr alloy shows obvious stress peaks and dynamic softening, and its rheological curve can be considered as DRX type. The flow stress initially increases rapidly, exhibiting a rapid work-hardening (WH) phenomenon, similarly to the stage I in Fig. 2b. Next, work-hardening rate decreases gradually, the stress reaches the peak and then slowly decreases continually to be of steady-state type as the strain increases. The significant dynamic softening shown is similar to stage II and stage III in Fig. 2b. In addition, the
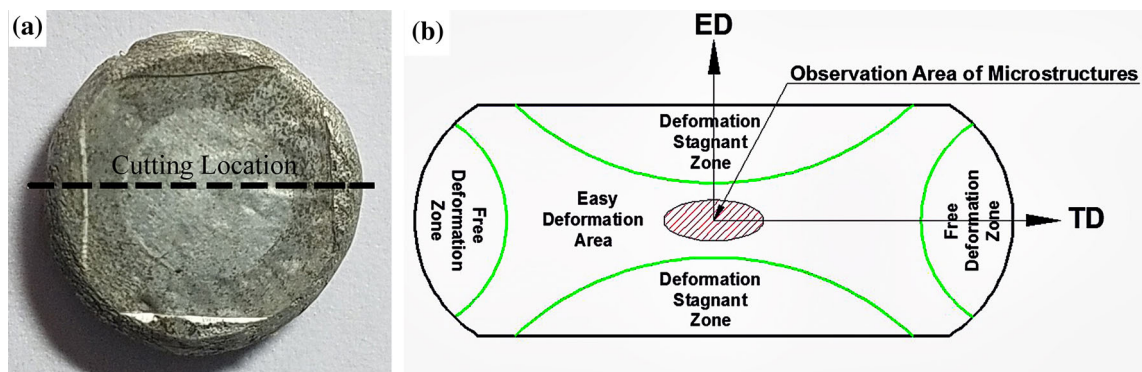

Figure 1 **a** Macrophotograph of the compressed sample, and **b** schematic of the longitudinal section of the compressed sample.
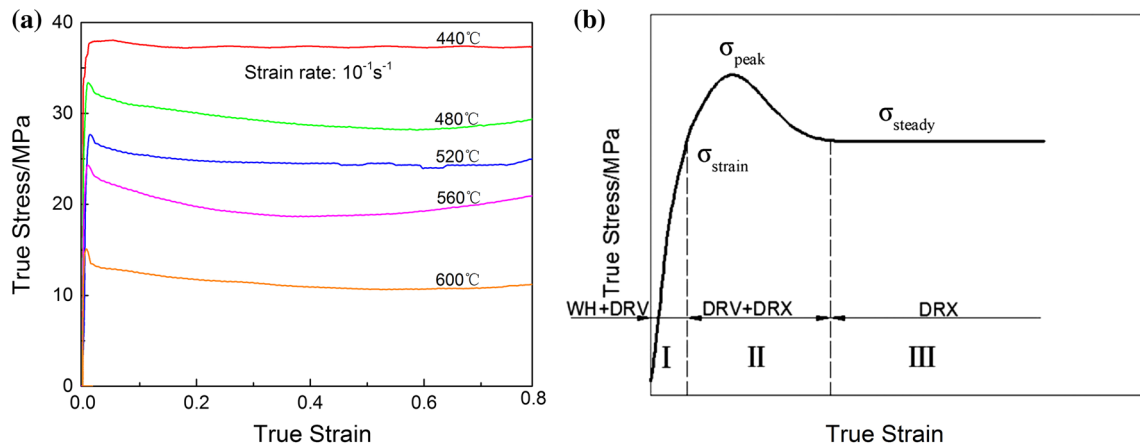
Figure 2 **a** True stress–strain curves at the strain rate of 0.1 s^{-1} at different temperatures and **b** sketch of typical DRX-type flow curve.

deforming temperature significantly affects the peak stress, which has obviously decrease with increasing of deformation temperature.

Effects of processing parameters on microstructures

Figure 3 shows the optical microstructures of the test alloy deformed at different temperatures and strain rates. For the annealed Al–0.2Sc–0.04Zr alloy, as
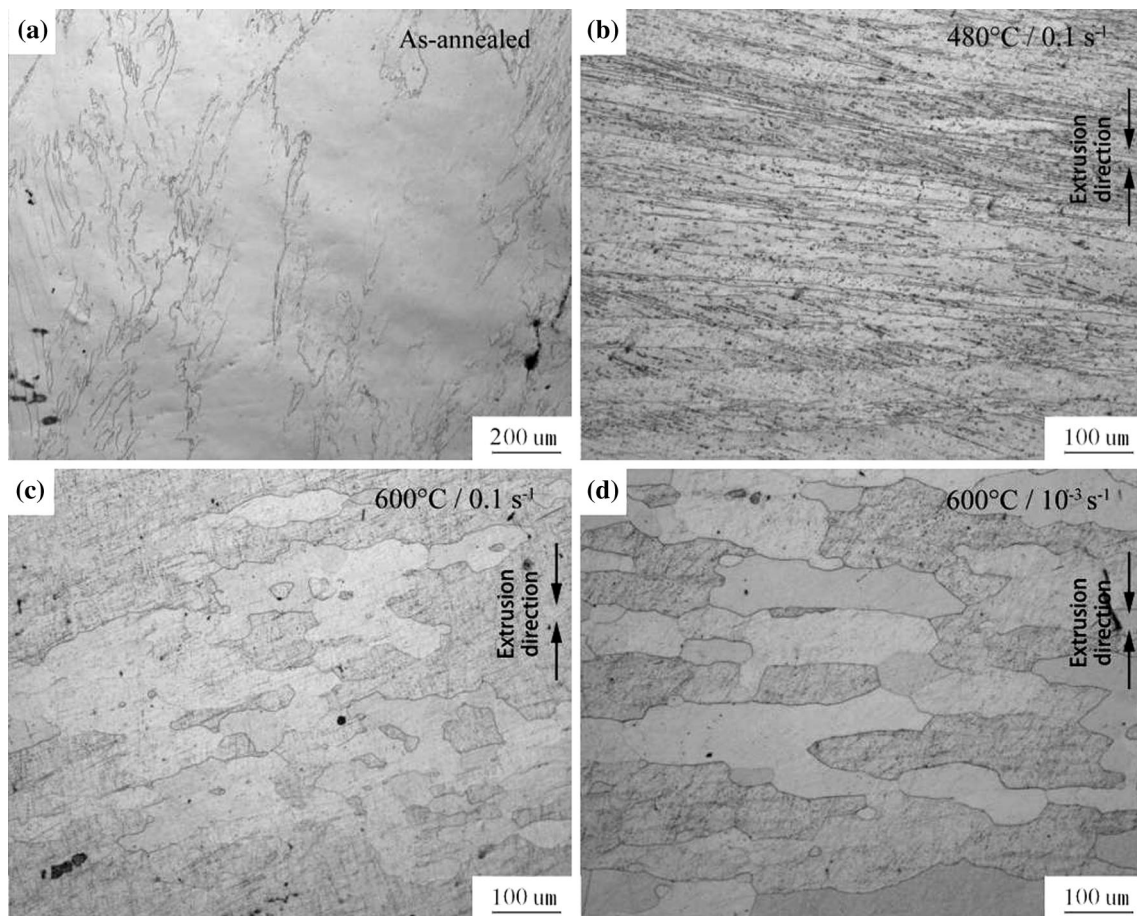
Figure 3 Optical microstructures of the samples under the various conditions: **a** as-annealed, **b** 480 °C/0.1 s^{-1}, **c** 600 °C/0.1 s^{-1}, and **d** 600 °C/10^{-3} s^{-1}.

shown in Fig. 3a, the grain size of structure is especially coarse. After thermal compression, as shown in the picture (Fig. 3b–d), the initial coarse grains are flattened and elongated along the direction vertical to the compression. From the comparative analysis of Fig. 3b, c, a dense and narrowly banded structure is observed in Fig. 3b. However, the banded structure is significantly coarsened in Fig. 3c. It is because that, at the high temperature of 600 °C, atoms become more active, and the climbing capabilities of both the cross slip of screw dislocations and edge dislocations increase, promoting DRX nucleation and growth [17]. From the comparative analysis of Fig. 3c, d, at 600 °C and low strain rate of 10^{-3} s^{-1}, the grain sizes of the banded structure become coarser and larger. It is because that more time for DRX nucleation and subsequent growth is available at low strain rates. At high strain rates, the driving force for DRX is increased [18], which increases the nucleation rate, and the excessively rapid strain rate does not provide sufficient time for the grains to grow. Thus, both deformation temperature and strain rate exhibit significant influences on the extent of DRX.

Processing map

Establishment and optimization of hot working domains

Figure 4a, b, respectively, shows the instability maps constructed using the Kumar–Prasad (K–P) and Murty–Rao (M–R) instability criteria. The white area represents the stable plastic flow region, while colorful areas I, II and III represent three unstable flow regions in Fig. 4. The obvious differences between the K–P and M–R instability maps can be clearly observed. Although the outlines of the three unstable regions identified by the M–R criterion are almost equivalent to those identified by the K–P criterion, each unstable region in Fig. 4b seems to shift an equal amount upward along the ordinate compared to unstable regions in Fig. 4a. The regions with strain rate range of 1–5 s^{-1} are identified by the both criteria as stable regions at all test temperatures. Therefore, this alloy demonstrates its applicability for deformation at high strain rates, such as those experienced during forging and pressing, rolling or wire drawing.

Figure 5a, b shows the processing maps constructed using the K–P and M–R instability/stability criteria, respectively. The gray-shaded regions in Fig. 5 represent the unstable flow regions. The curves in Fig. 5 represent iso-η contours. The prediction results of two types of processing maps were examined by the as follows. The flow stability of the deformed sample was confirmed by microscopic observation. And then it was compared with the prediction results of two types of processing maps to confirm the deformation conditions of the deformed samples. Four key points in both maps were selected to examine the accuracy of the K–P and M–R processing maps with the aid of microstructure observation.

These selected points, which marked as A, B, C and D, represented the following four different deformation conditions: 480 °C/10^{-3} s^{-1}, 600 °C/10^{-3} s^{-1}, 480 °C/10^{-2} s^{-1}, and 560 °C/10^{-2} s^{-1}, respectively. Points A and B were located in the unstable region of the K–P processing map (Fig. 5a) but were located in
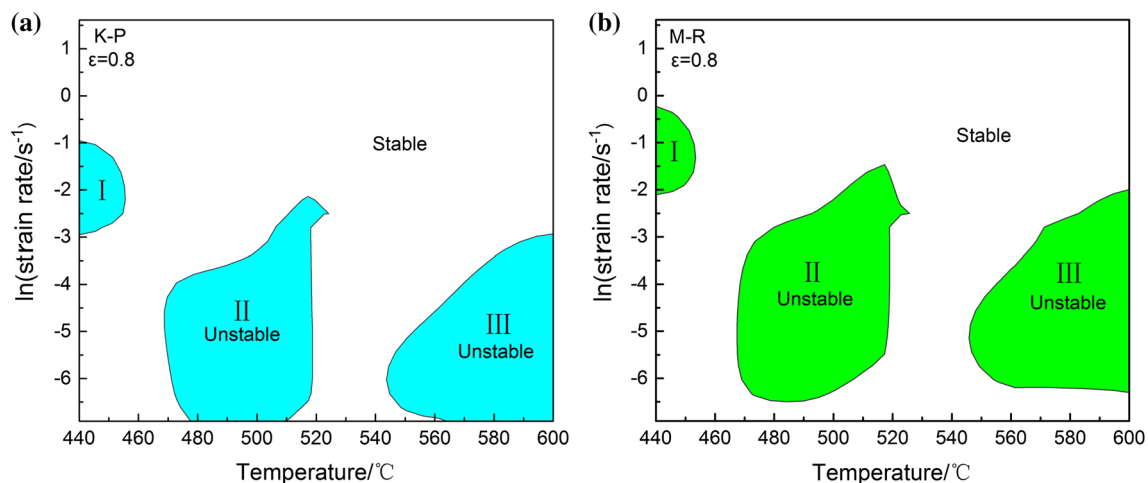

Figure 4 Instability maps constructed using the a K–P and b M–R instability criteria at the true strain of 0.8.
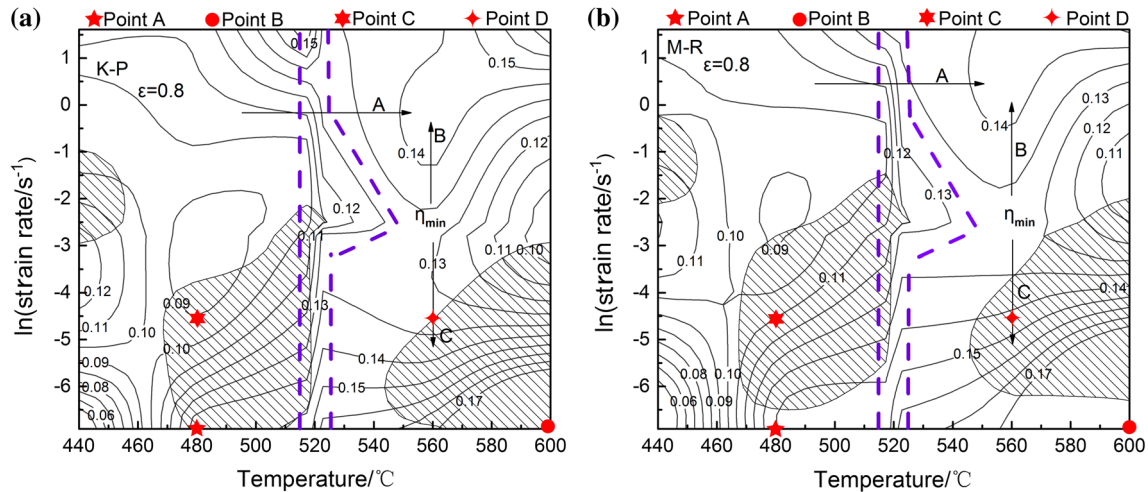
Figure 5 Processing maps constructed using the **a** K–P and **b** M–R criteria at the true strain of 0.8.

the stable flow region of the M–R processing map (Fig. 5b). Point D was located in the stable region of the K–P processing map (Fig. 5a) but was located in the unstable region of the M–R processing map (Fig. 5b). Point C was located in the unstable region of both the K–P and M–R processing maps.

*Analysis of processing maps*

The significant influence of temperature and strain rate on the dynamic energy consumption behavior of the alloy leads to significant changes in power dissipation efficiency. It can be seen from Fig. 5 that although the values of power dissipation increase with decreasing strain rate or increasing deformation temperature, the η value is relatively low. For the metals or alloys with high stacking fault energy, especially the aluminum alloys, higher power dissipation efficiency is needed for a completed DRX, because of the difficulty in dislocation entanglement and accumulation, as well as new grain nucleation. Numerous studies have also shown that when the η is greater than 0.3, the alloy will exhibit complete DRX during thermoforming. Therefore, the reasons for the decrease in the η are explained by two aspects.

For different Al alloys, the composition has a great influence on the power dissipation efficiency. Zhang [19] reported that in Al–Mn–Mg–RE alloy, η can reach 0.38. For the 2050 Al–Li alloy, the η is between 0.28 and 0.33 under the optimum processing conditions [20]. However, the η of Al–Si–Mg alloy is only 0.18–0.23 [21]. Therefore, the properties of different types of aluminum alloys are greatly affected in this

respect. On the other hand, for Al–Sc alloys, Sc can effectively resist recrystallization. This greatly affects the power dissipation efficiency, causing the value of the η to decrease.

Jia et al. [6]. pointed out that the recrystallization temperature of the Al–0.11%Zr alloy without Sc is 250 °C, while the addition of 0.15%Sc (Al–0.15%Sc–0.11%Zr) raises the recrystallization temperature to near 600 °C. Figure 6a–c show SEM images of the samples deformed at 440 °C/1 s^{-1} and 600 °C/0.01 s^{-1} and EDS analysis, respectively. From EDS analysis shown in Fig. 6c, the white particles shown in Fig. 6a, b are identified as the precipitated phase of Al$_3$(Sc,Zr). The SEM images show that precipitate particles with the diameter of less than 100 nm exhibit extremely disperse and dense distribution and that these particles are not coarsened as deformation temperature rises from 440 to 600 °C. During plastic deformation, there are generally two ways of interaction between moving dislocations and the precipitate particles, the precipitate shearing mechanism and the Orowan dislocation bypass mechanism. Fuller et al. [22]. found that, when diameter of Al$_3$(-Sc,Zr) precipitates is less than 4 nm, the precipitate shearing mechanism is dominant, otherwise, the Orowan dislocation bypass mechanism is dominant. From Fig. 6a, b, during plastic deformation, no matter precipitate shearing or the Orowan bypass mechanism occurs, these nano-dimension particles can forcefully hinder the movement of dislocation and grain boundary, effectively resist recrystallization and increase consumption of extra power [6], resulting in the increase in thermal stability and the

Figure 6 SEM images of the samples after hot compression at **a** 440 °C/1 s^{-1} and **b** 600 °C/10^{-2}s^{-1}, and **c** energy dispersion spectrum analysis results.
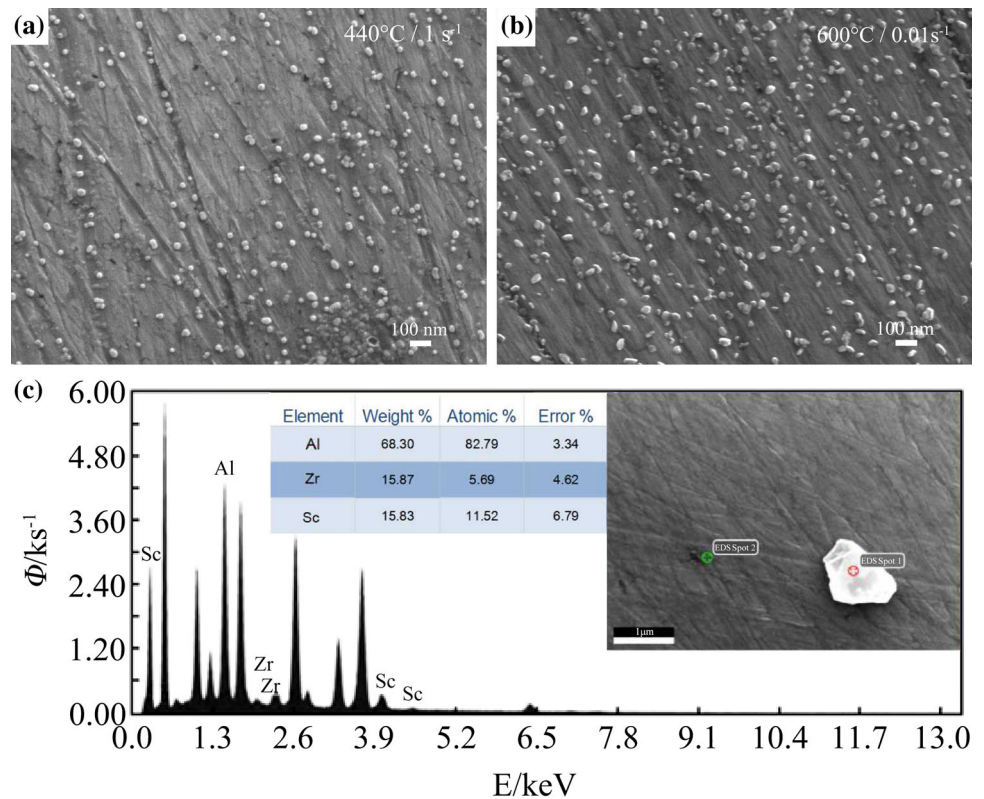
universal decrease in η values in processing map (Fig. 5).

Figure 7 shows the EBSD grain maps of the samples deformed at the above four conditions (Points A, B, C and D). The grain tolerance angle and the minimum grain size were set to 5° and 2, respectively, in the TSL-OIM software to produce the EBSD grain maps. After deformation under the condition of Point A, a mixed structure of coarse grains and fine grains is observed in Fig. 7a. New recrystallized grains were generated at grain boundaries of coarse grains. Coarse grains with a uniform distribution were surrounded by fine equiaxed grains. These features indicate the occurrence of steady DRX [23]. It is confirmed that Point A is located in the stable region. Figure 7b shows the grain map of the sample deformed under the condition of Point B. Because of the high deformation temperature, atoms become more active, and the driving force behind grain boundary movement is larger, promoting grains to swallow surrounding grains and grow rapidly [24]. Eventually, a coarse and uniformly distributed structure is formed, and Point B is also verified to be located in the stable deformation region. Figure 7c, d shows the EBSD grain maps of the studied samples

deformed under the conditions of Points C and D, respectively. In both maps, flow localization and adiabatic shear band (ASB) can be clearly observed. The severe local flow occurred at the center of the ASB, where very fine equiaxed grains were formed. Grains in the transition zone and matrix were relatively larger and coarser. This extremely nonuniform microstructures indicates the occurrence of unstable deformation [25]. Local deformation generally begins in the boundaries of coarse grains, causing the formation of flow localization and ASB [26]. So both Points C and D were verified to be located in the unstable deformation region. The microstructure examination of the four selected points further demonstrates the accuracy of the processing map constructed using the M–R criterion.

In general, iso-η contours in a processing map continuously change. η-contours reflect the given microstructure change over the certain ranges of temperature and strain rate, namely, the microstructure evolution tracks [27, 28]. From Fig. 5a, b, it can be observed that the η values in both maps were low, and distinct curvature changes in the contours appear at entire strain rates at 520 °C, as shown in blue dotted line area. This implies that there occurred
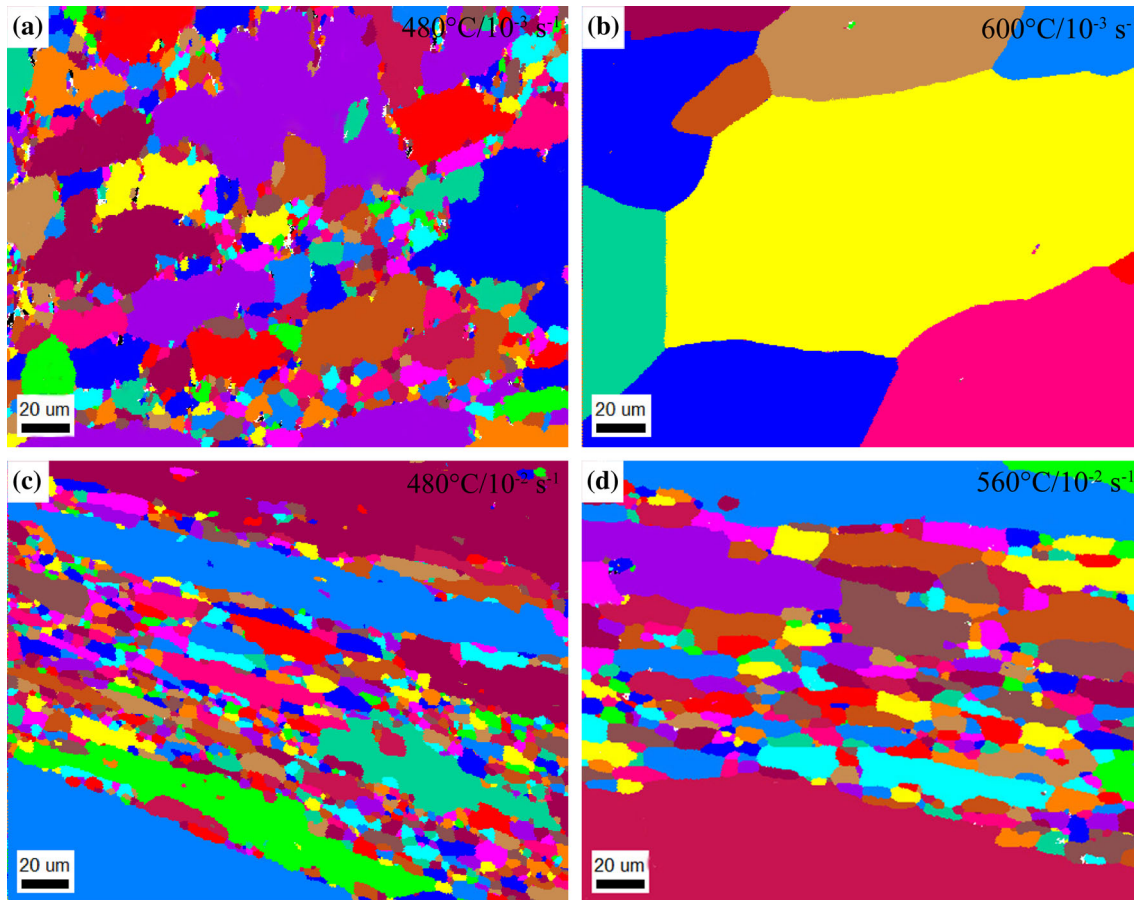
Figure 7 Grain maps displayed by random colors under the different deformation conditions: **a** 480 °C/10^{-3} s^{-1}, **b** 600 °C/10^{-3} s^{-1}, **c** 480 °C/10^{-2} s^{-1} and **d** 560 °C/10^{-2} s^{-1}.

deformation mechanism change near 520 °C. From the microstructure evolution captured by EBSD, the region near 520 °C happens to be the transition zone of the microstructure change from predominantly DRV to predominantly DRX. So, the blue dotted line area in Fig. 5 is named DRV–DRX boundary belt. From the left of the boundary belt to its right, as shown at the arrow A, the η values increased rapidly. In addition, η-contours near $T = 520$ °C and $\dot{\varepsilon} = 0.1$ s^{-1} on the boundary belt extend toward higher temperature zone. The η value at 520 °C and 0.1 s^{-1} drops to a minimum value compared to the η value at 520 °C and other strain rates. In the same way, the lowest η value also appeared at strain rate of 0.1 s^{-1} at 540 °C and 560 °C compared to the η value at other strain rates. The arrows A, B and C in Fig. 5 show the directions of these arrows were consistent with the directions of increasing η value. Figure 8 supports this phenomenon as well by showing a larger fraction of recovered structure after deformation at 560 °C

and 0.1 s^{-1}. It can be seen that, at the strain rate of 0.1 s^{-1}, full DRX was still difficult to achieve even at high temperature of 560 °C.

Microstructure evolution

The inverse pole figure maps of the samples deformed at 560 °C and 0.1 s^{-1} and 5 s^{-1} are shown in Fig. 8. As shown in Fig. 8a, at low strain rate of 0.1 s^{-1}, a mainly recovered and partially recrystallized structure is observed, whereas at high strain rate of 5 s^{-1}. As shown in Fig. 8b, a completely dynamically recrystallized structure with new strain-free grains is observed, and the recrystallized grain size was slightly larger. Figure 9c shows variation in the grain orientation spread (GOS) values, average kernel average misorientation (KAM) values and DRX grain size at 560 °C with strain rate. An initial decrease followed by an increase in recrystallized grain size was observed as the strain rate increases

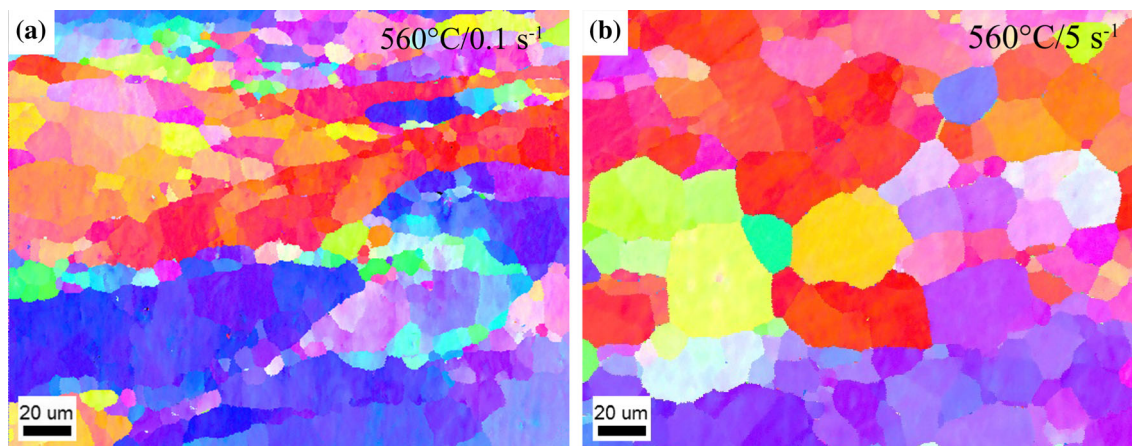**Figure 8** Inverse pole figure maps of the samples compressed at 560 °C at strain rates of **a** 0.1 s^{-1} and **b** 5 s^{-1}.
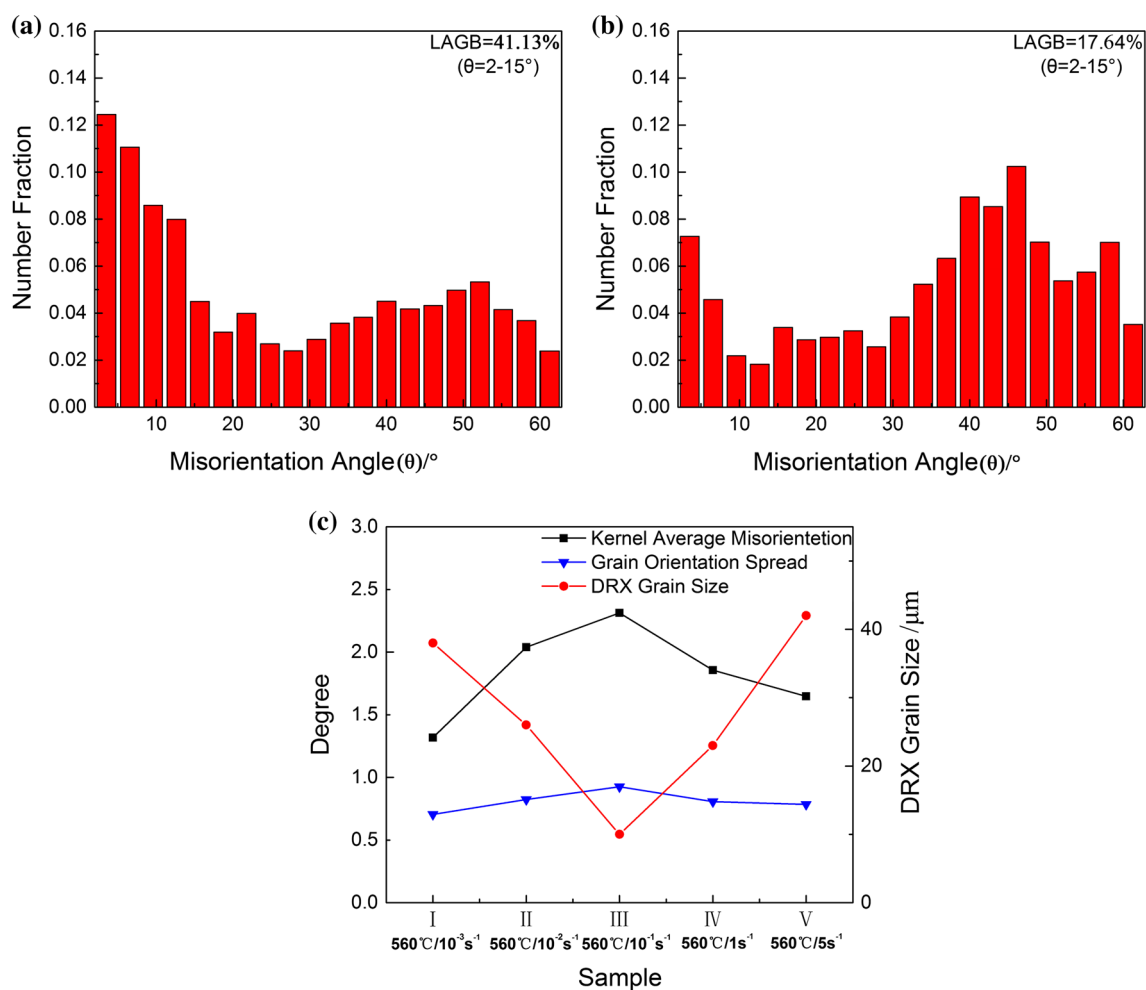

Figure 9 Misorientation angles of the samples compressed at 560 °C at strain rates of **a** 0.1 s^{-1} and **b** 5 s^{-1} and **c** evolution of intragranular misorientation and DRX grain size.

for the alloy at 560 °C, as shown in Fig. 9c. Nayan et al. [23] obtained a similar variation trend in their

study and assumed that adiabatic temperature rise (ATR) facilitates the occurrence of DRX at high
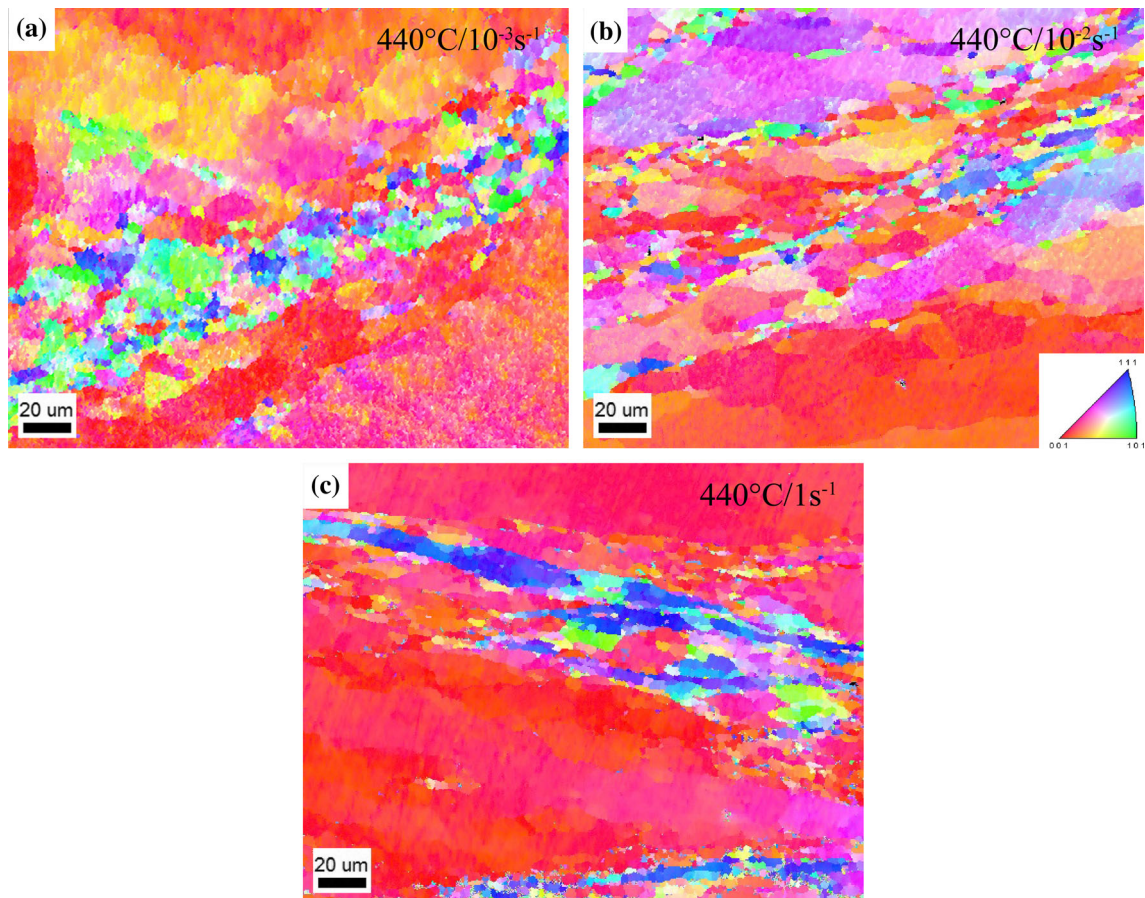
Figure 10 Inverse pole figure maps of the samples compressed at 440 °C at strain rates of **a** 10^{-3} s^{-1}, **b** 10^{-2} s^{-1} and **c** 1 s^{-1}.

deformation temperature and high strain rate. Because the high kinetic energy of the atoms caused by ATR promotes rapid nucleation and growth of new strain-free grains via reconstitution of the microstructure. This explanation can be further supported by the aid of the variation trends of η value shown in Fig. 5 and KAM and GOS shown in Fig. 9c. As shown in Fig. 9c, using $\dot{\varepsilon} = 0.1$ s^{-1} as the dividing point, the KAM and GOS values increase firstly and then decrease with increasing strain rate. The η value at 560 °C decreases firstly and then increases with increasing strain rate, as shown in Fig. 5. Their variation trends have a high agreement with the microstructure evolution at 560 °C with strain rate. The gradual increases in the KAM and GOS values at 560 °C and $\dot{\varepsilon} < 0.1$ s^{-1}. Figure 9c indicates the increase in dislocation content, especially the number of geometrically necessary dislocations in the structure, with increasing strain rate [23]. However, at 560 °C and $\dot{\varepsilon} > 0.1$ s^{-1}, a gradually increasing fraction of DRX with increasing strain rate caused a decrease in

the overall dislocation density inside the grains due to the formation of new strain-free grains. From the comparative analysis of Fig. 9a, b, the sample deformed at 560 °C and 0.1 s^{-1} shows the presence of a higher fraction of low-angle grain boundaries (LAGB, $\theta = 2$–15°). Besides, as shown in Fig. 5, η value at 0.1 s^{-1} drops to its minimal value, which can be confirmed from the limited DRX structure shown in Fig. 8a. In contrast, at higher strain rate of 5 s^{-1}, the ATR promoted DRX nucleation and grain growth, facilitating the formation of strain-free grains with high-angle grain boundaries, as shown in Fig. 8b.

Figure 10 shows the inverse pole figure maps of the samples deformed at 440 °C at three different strain rates of 10^{-3}, 10^{-2} and 1 s^{-1}. In view of the overall situation, a mainly recovered and partially recrystallized structure is observed after low-temperature deformation. At lower strain rates, as shown in Fig. 10a, the inverse pole figure of the deformed sample shows a slightly larger fraction of
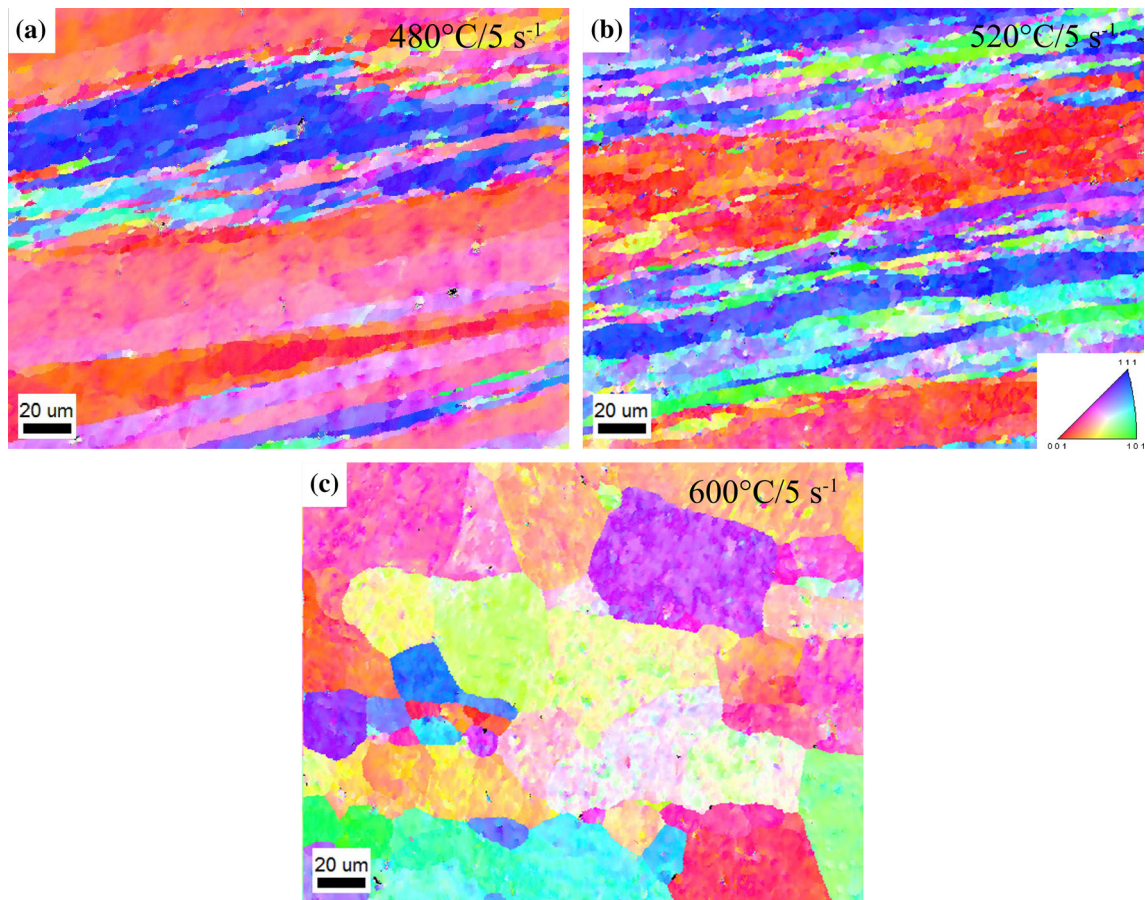
Figure 11 Inverse pole figure maps of the samples compressed at strain rate of 5 s^{-1} at **a** 480 °C, **b** 520 °C and **c** 600 °C.

recrystallized structure with high-angle grain boundaries, and the recrystallized grain size of DRX is also slightly larger. The fraction of DRX decreases gradually as the strain rate increases from 10^{-3} to 1 s^{-1}. At low temperature and high strain rate, due to the limited kinetic energy of the atoms and limited time available for dislocation interaction and rearrangement, the process of conversion from low-angle dislocation boundary to high-angle grain boundary was more incomplete, which limited the process of DRX. DRX generally begins at high-angle grain boundaries, and subsequent nucleation of new grains occurs at the boundaries of growing grains [29, 30].

Figures 11 and 8b are used to analyze the inverse pole figure maps of the samples deformed at a strain rate of 5 s^{-1} at four different temperatures (480 °C, 520 °C, 560 °C and 600 °C). It can be easily observed that the extent of DRX increases significantly with increasing deformation temperature. At the high strain rate of 5 s^{-1} and lower temperatures of 480 °C (Fig. 11a) and 520 °C (Fig. 11b), deformation banding

and orientation gradients are clearly presented in their structures. The presence of wavy grain boundaries between the banded structures indicates the occurrence of DRX. However, the DRX is extremely incomplete, and partial coarse and elongated recovered structure remains. At higher temperatures of 560 °C (Fig. 8b) and 600 °C (Fig. 11c), the extent of DRX and recrystallized grain size increase significantly and the microstructure exhibits a strain-free equiaxed grain distribution with a random grain orientation, which indicates the occurrence of full DRX. In addition, microstructures of the samples deformed at 480 °C and 520 °C (Fig. 11a, b) show higher intragranular misorientation compared to those of the samples deformed at 560 °C (Fig. 8b) and 600 °C (Fig. 11c). Therefore, the deformation temperature is observed to have a significant impact on the extent of DRX [31].

To sum up, the complex nature of microstructure evolution was evident from EBSD analysis, which successfully captured the microstructure evolution of
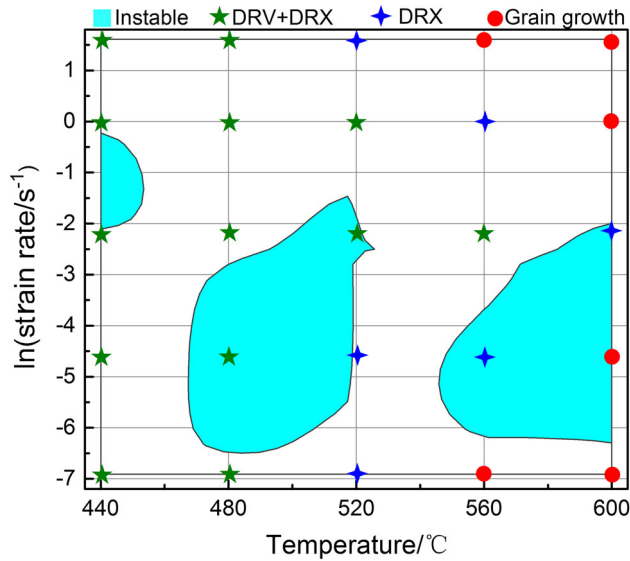
Figure 12 Deformation mechanism map constructed at the true strain of 0.8.

the Al–0.2c–0.04Zr alloy over a wide range of strain rates and temperatures. Based on the microstructure evolution and the M–R processing map of Al–0.2c–0.04Zr, a deformation mechanism map applicable for this alloy was developed, as shown in Fig. 12. The deformation mechanism map and the M–R processing map (Fig. 5b) show that the optimum temperature T and strain rate $\dot{\varepsilon}$ combination conditions for Al–0.2Sc–0.04Zr alloy are $T = 520$–560 °C, $\dot{\varepsilon} = 10^{-3}\,\text{s}^{-1}$ or $\dot{\varepsilon} = 0.1$–$5\,\text{s}^{-1}$. The microstructure evolution dominated by the predominant or complete dynamic recrystallization can be acquired by deformation at the combination conditions. However, it is dominated mainly by dynamic recovery at lower temperatures ($T < 520$ °C) and by dynamic recrystallization at higher temperatures ($T > 520$ °C). In addition, the microstructure of specimen deformed at 600 °C shows a growing and coarse trend. The region ranges of $\dot{\varepsilon} = 0.015$–$0.135\,\text{s}^{-1}$, $T = 470$–520 °C or $T = 550$–600 °C are the main unstable regions prone to the deformation localization.

Conclusions

1. The flow stress of the Al–0.2Sc–0.04Zr alloy deformed at elevated temperatures has a rapid increase to the maximum stress, subsequently, the flow stress decreases continually to be of steady-state type when the deformation

continues on. In addition, the deforming temperature significantly affects the peak stress, which has obviously decreased with increasing of deformation temperature.

2. For the Al–0.2Sc–0.04Zr alloy deformed at elevated temperatures, the M–R criterion can more accurately predict the unstable region than the K–P criterion.

3. The optimum temperature T and strain rate $\dot{\varepsilon}$ combination conditions for the test alloy are $T = 520$–560 °C, $\dot{\varepsilon} = 10^{-3}\,\text{s}^{-1}$ or $\dot{\varepsilon} = 0.1$–$5\,\text{s}^{-1}$. And the region ranges of $\dot{\varepsilon} = 0.015$–$0.135\,\text{s}^{-1}$, $T = 470$–520 °C or $T = 550$–600 °C are the main unstable regions prone to the deformation localization.

4. Both deformation temperature and strain rate exhibit a significant influence on the extent of DRX. The microstructure evolution dominated by the predominant or complete dynamic recrystallization can be acquired by deformation at the combination conditions ($T = 520$–560 °C, $\dot{\varepsilon} = 10^{-3}\,\text{s}^{-1}$ or $\dot{\varepsilon} = 0.1$–$5\,\text{s}^{-1}$). However, it is dominated mainly by dynamic recovery at lower temperatures ($T < 520$ °C) and by dynamic recrystallization at higher temperatures ($T > 520$ °C). In addition, the microstructure of specimen deformed at 600 °C shows a growing and coarse trend.

5. The nano-dimension precipitate particles of Al_3(-Sc,Zr) are uniformly distributed throughout Al matrix. The efficiency parameter η value of Al–0.2Sc–0.04Zr alloy in processing map is smaller in comparison with that in pure aluminum, it could be attributed to these nano-dimension particles.

Acknowledgements

Compliance with ethical standards

Conflict of interest We declare that we have no financial and personal relationships with other people or organizations that can inappropriately influence our work, there is no professional or other personal interest of any nature or kind in any

product, service and/or company that could be construed as influencing the position presented in, or the review of, the manuscript entitled.

References

[1] Chao RZ, Guan XH, Guan RG, Tie D, Lian C, Wang X, Zhang J (2014) Effect of Zr and Sc on mechanical properties and electrical conductivities of Al wires. Trans Nonferrous Metals Soc China 24(10):3164–3169

[2] Li ZH, Cai B, Liu Q, Qian HL (2010) Ageing strengthening and electrical conductivity of Al–xSc–0.04Zr (x = 0, 0.1%, 0.2% and 0.4%). Spec Cast Nonferrous Alloys 30(5):476–480

[3] Li J, Cai B, Zhou W (2011) Aging behavior and electric conductivity of a new heat resistant Al–0.2Sc–0.04Zr (0.01B) alloy. Spec Cast Nonferrous Alloys 31(11):1070–1073

[4] Song M, He Y, Fang S (2011) Effects of Zr content on the yield strength of an Al–Sc alloy. J Mater Eng Perform 20(3):377–381

[5] Zhou WW, Cai B, Li WJ, Liu ZX, Yang S (2012) Heat-resistant Al–0.2Sc–0.04Zr electrical conductor. Mater Sci Eng A 552(34):353–358

[6] Jia ZH, Røyset J, Solberg JK, Liu Q (2012) Formation of precipitates and recrystallization resistance in Al–Sc–Zr alloys. Trans Nonferrous Metals Soc China 22(8):1866–1871

[7] Du G, Deng JW, Yan DS, Zhao MJ, Rong LJ (2009) Coarsening behavior of Al3(Sc, Zr) precipitates and its influence on recrystallization temperature of Al–Mg–Sc–Zr Alloy. J Mater Sci Technol 25(6):749–752

[8] Cai B, Li W, Zhou W, Li J, Li Z (2014) High temperature creep behavior of Al–0.2Sc–0.04Zr alloy. Spec Cast Nonferrous Alloys 34(2):113–115

[9] Babu KA, Mandal S, Kumar A, Athreya CN, de Boer B, Sarma VS (2016) Characterization of hot deformation behavior of alloy 617 through kinetic analysis, dynamic material modeling and microstructural studies. Mater Sci Eng A 664:177–187

[10] Kotkunde N, Krishnamurthy HN, Singh SK, Jella G (2018) Experimental and numerical investigations on hot deformation behavior and processing maps for ASS 304 and ASS 316. High Temp Mater Process (Lond) 37:9–10

[11] Çadırlı E, Tecer H, Şahin M, Yılmaz E, Kırındı T, Gündüz M (2015) Effect of heat treatments on the microhardness and tensile strength of Al–0.25wt.% Zr alloy. J Alloys Compd 632:229–237

[12] Knipling KE, Karnesky RA, Lee CP, Dunand DC, Seidman DN (2010) Precipitation evolution in Al–0.1Sc, Al–0.1Zr and Al–0.1Sc–0.1Zr (at.%) alloys during isochronal aging. Acta Mater 58(15):5184–5195

[13] Murty SVSN, Rao BN (1998) On the development of instability criteria during hotworking with reference to IN 718. Mater Sci Eng A 254(1–2):76–82

[14] Babu NS, Tiwari SB, Rao BN (2013) Modified instability condition for identification of unstable metal flow regions in processing maps of magnesium alloys. Mater Sci Technol 21(8):976–984

[15] Lin YC, Chen XM, Wen DX, Chen MS (2014) A physically-based constitutive model for a typical nickel-based superalloy. Comput Mater Sci 83(2):282–289

[16] Lin YC, Chen MS, Zhong J (2008) Constitutive modeling for elevated temperature flow behavior of 42CrMo steel. Comput Mater Sci 42(3):470–477

[17] Xie J, Zhu Y, Bian F, Liu C (2017) Dynamic recovery and recrystallization mechanisms during ultrasonic spot welding of Al–Cu–Mg alloy. Mater Charact 132:145–155

[18] Yang Q, Deng Z, Zhang Z, Liu Q, Jia ZH, Huang GJ (2016) Effects of strain rate on flow stress behavior and dynamic recrystallization mechanism of Al–Zn–Mg–Cu aluminum alloy during hot deformation. Mater Sci Eng A 662:204–213

[19] Zhang T, Tao YR, Wang XY (2014) Constitutive behavior, microstructural evolution and processing map of extruded Al–1.1Mn–0.3Mg–0.25RE alloy during hot compression. Trans Nonferrous Metals Soc China 24(5):1337–1345

[20] Zhu RH, Liu Q, Li JF, Chen YL, Zhang XH, Zheng ZQ (2018) Flow curve correction and processing map of 2050 Al–Li alloy. Trans Nonferrous Metals Soc China 28(3):404–414

[21] Lin YC, Luo SC, Jiang XY, Tang Y, Chen MS (2018) Hot deformation behavior of a Sr-modified Al–Si–Mg alloy: constitutive model and processing maps. Trans Nonferrous Metals Soc China 28(4):592–603

[22] Fuller CB, Seidman DN, Dunand DC (2003) Mechanical properties of Al(Sc,Zr) alloys at ambient and elevated temperatures. Acta Mater 51(16):4803–4814

[23] Nayan N, Murty SVSN, Chhangani S, Prakash A, Prasad MJNV, Samajdar I (2017) Effect of temperature and strain

rate on hot deformation behavior and microstructure of Al–Cu–Li alloy. J Alloy Compd 723:548–558

[24] Zhang JS, Xia YF, Quan GZ, Wang X, Zhou J (2018) Thermal and microstructural softening behaviors during dynamic recrystallization in 3Cr20Ni10W2 alloy. J Alloy Compd 743:464–478

[25] Kozmel T, Vural M, Tin S (2016) EBSD characterization of shear band formation in aluminum armor alloys. J Mater Sci 51(16):7554–7570. https://doi.org/10.1007/s10853-016-0035-0

[26] Yiadom SB, Khan AK, Bassim N (2014) Effect of microstructure on the nucleation and initiation of adiabatic shear bands (ASBs) during impact. Mater Sci Eng A 615:373–394

[27] Kumar AKSK, Rao BN (1998) Ziegler's criterion on the instability regions in processing maps. J Mater Sci Lett 17(14):1203–1205

[28] Prasad YVRK, Gegel HL, Doraivelu SM, Malas JC, Morgan JT, Lark KA, Barker DR (1984) Modeling of dynamic material behavior in hot deformation: forging of Ti-6242. Metall Trans A 15(10):1883–1892

[29] Humphreys FJ, Hatherly M (2004) Chapter 14 in recrystallization and related annealing phenomena, 2nd edn. Elsevier, London, pp 451–467

[30] Hakamada M, Watazu A, Saito N, Iwasaki H (2008) Dynamic recrystallization behavior during compressive deformation in Mg–Al–Ca–RE alloy. J Mater Sci 43(6):2066–2068. https://doi.org/10.1007/s10853-008-2474-8

[31] Wang WY, Pan QL, Sun YW, Wang XD, Li A, Song WB (2016) Study on hot compressive deformation behaviors and corresponding industrial extrusion of as-homogenized Al–7.82Zn–1.96Mg–2.35Cu–0.11Zr alloy. J Mater Sci 53(16):11728–11748. https://doi.org/10.1007/s10853-018-2388-z